ARTICLES
https://doi.org/10.1038/s41563-021-00968-7

nature materials

Check for updates

Spin-induced linear polarization of photoluminescence in antiferromagnetic van der Waals crystals

Xingzhi Wang[1]✉, Jun Cao[1], Zhengguang Lu[2,3], Arielle Cohen[4], Hikari Kitadai[1], Tianshu Li[4], Qishuo Tan[1], Matthew Wilson[5], Chun Hung Lui[5], Dmitry Smirnov[2], Sahar Sharifzadeh[1,4,6,7] and Xi Ling[1,4,8]✉

Antiferromagnets are promising components for spintronics due to their terahertz resonance, multilevel states and absence of stray fields. However, the zero net magnetic moment of antiferromagnets makes the detection of the antiferromagnetic order and the investigation of fundamental spin properties notoriously difficult. Here, we report an optical detection of Néel vector orientation through an ultra-sharp photoluminescence in the van der Waals antiferromagnet $NiPS_3$ from bulk to atomically thin flakes. The strong correlation between spin flipping and electric dipole oscillator results in a linear polarization of the sharp emission, which aligns perpendicular to the spin orientation in the crystal. By applying an in-plane magnetic field, we achieve manipulation of the photoluminescence polarization. This correlation between emitted photons and spins in layered magnets provides routes for investigating magneto-optics in two-dimensional materials, and hence opens a path for developing opto-spintronic devices and antiferromagnet-based quantum information technologies.

Since the discovery of monolayer ferromagnets, magneto-optics has played a compelling role in revealing new physics of magnetism in the extreme nanoscale limit[1–3]. For example, the spin orientation in two-dimensional (2D) ferromagnets can be detected using the magneto-optical Kerr effect[1,2] or spontaneous circularly polarized photoluminescence (PL)[4]. Compared to ferromagnets, however, studies of magneto-optics in 2D antiferromagnets are far more difficult due to the lack of net magnetic moments[5,6], despite their appealing nature for next-generation spintronic devices[7–12]. Raman spectroscopy[13–15] and second harmonic generation[16,17] have been applied to detect the presence of spin structure in 2D antiferromagnets, based on the expansion of the unit cell and the breaking of the centrosymmetry of materials. Nevertheless, these methods are not sufficient to provide fine information of spin properties in 2D antiferromagnets, such as the local Néel vector orientation[13–16]. One promising strategy to investigate the spin properties in 2D antiferromagnets is to leverage a coupling between spins and other excitation elements, which do not rely on the stray fields of spins.

The monolayer $NiPS_3$ crystal has a hexagonal lattice structure with three-fold rotational symmetry, and thus it is reasonable to expect it to exhibit distinctive in-plane isotropic properties (Supplementary Fig. 1a)[18,19]. Such in-plane isotropy is largely retained in monoclinic bulk $NiPS_3$ due to the weak interlayer coupling, though the interlayer stacking order in principle breaks the three-fold rotational symmetry[15,18]. For instance, bulk $NiPS_3$ exhibits a similar isotropic Raman response as do the monolayers[15]. However, when $NiPS_3$ transitions from the paramagnetic phase to the antiferromagnetic phase across its Néel temperature (T_N, ~152 K), the spins are aligned either in parallel or antiparallel along the in-plane *a* axis with a small out-of-plane component, as shown in Fig. 1a (ref. [20]). In each single layer, both the spin orientation and the zigzag ferromagnetic chains make the *a* axis different from the other two directions rotated by ±120°, and hence the three-fold rotational symmetry is broken. The Néel vector (that is, the antiferromagnetic vector) in the antiferromagnets is defined as $\mathbf{L}=\mathbf{M}_1-\mathbf{M}_2$, where $\mathbf{M}_1$ and $\mathbf{M}_2$ represent two oppositely aligned spins (Fig. 1b). As a consequence, the Néel vector in $NiPS_3$ also orients mainly along the *a* axis of the lattice.

Here, we report an observation of spin-correlated PL in van der Waals (vdW) antiferromagnetic $NiPS_3$ from bulk to trilayer flakes. The PL peak exhibits excellent monochromaticity with a near-intrinsic linewidth (~330 μeV at temperature *T* of ~5 K) in the near-infrared range (with photon energy of ~1.476 eV). Notably, the sharp emission shows a linear polarization correlated to the Néel vector orientation of $NiPS_3$, supported by the temperature- and magnetic-field-dependent spectroscopic study. Such a spin-correlated emission as that demonstrated in our study allows us to expediently read the spin properties in the bulk and atomically thin $NiPS_3$ flakes using steady-state spectroscopy, and provides concepts in the design of opto-spintronics in 2D systems.

Ultra-sharp emission from antiferromagnetic $NiPS_3$

Atomically thin $NiPS_3$ flakes are mechanically exfoliated from the high-quality $NiPS_3$ bulk single crystals (Fig. 1c and Supplementary Fig. 1). Figure 1d shows typical PL spectra of bulk and trilayer $NiPS_3$ under 568 nm continuous-wave laser excitation at a *T* of ~5 K. A distinctly sharp peak (labelled as X) is resolved at ~1.476 eV in the spectra of both the bulk and trilayer samples. The trilayer PL energy is only slightly (~0.8 meV) higher than the bulk PL energy, and

[1]Department of Chemistry, Boston University, Boston, MA, USA. [2]National High Magnetic Field Laboratory, Tallahassee, FL, USA. [3]Department of Physics, Florida State University, Tallahassee, FL, USA. [4]Division of Materials Science and Engineering, Boston University, Boston, MA, USA. [5]Department of Physics and Astronomy, University of California, Riverside, CA, USA. [6]Department of Electrical and Computer Engineering, Boston University, Boston, MA, USA. [7]Department of Physics, Boston University, Boston, MA, USA. [8]The Photonics Center, Boston University, Boston, MA, USA. ✉e-mail: xzwang@bu.edu; xiling@bu.edu

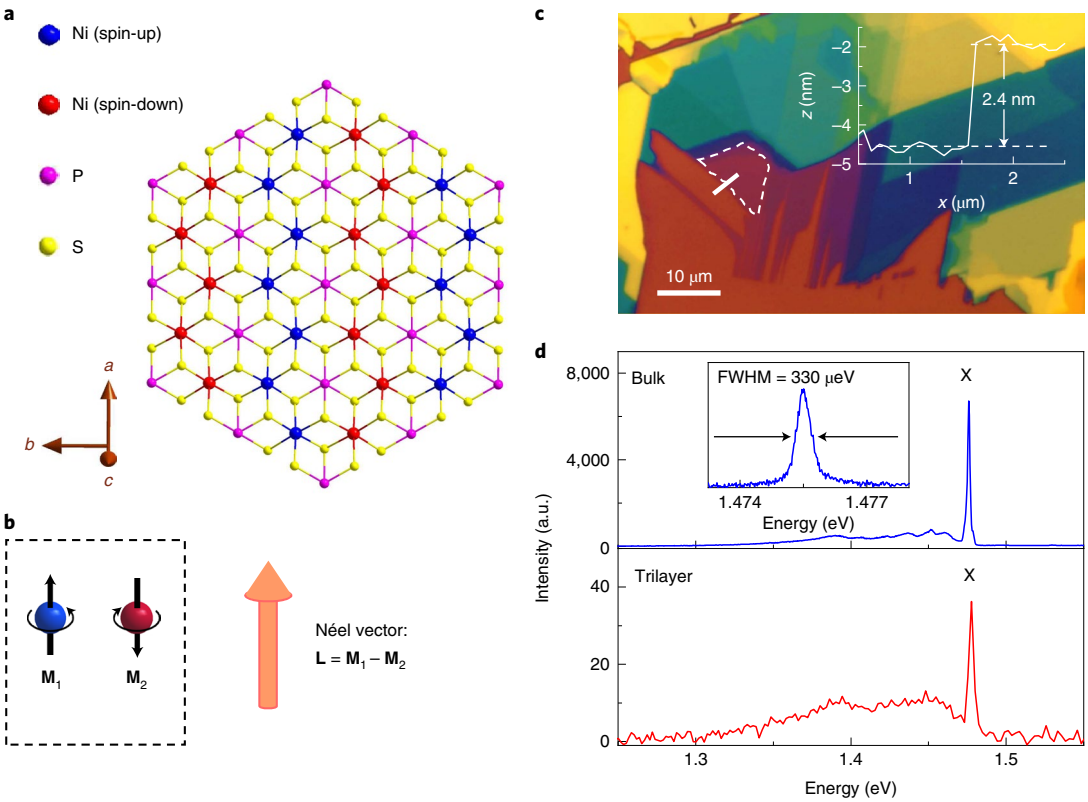

Fig. 1 | Antiferromagnetic spin structure and sharp emission of $NiPS_3$. **a**, Top view of spin structure of vdW antiferromagnet $NiPS_3$. The crystal orientations (*a*, *b* and *c* axes) are labelled by brown arrows. The spin orientation is mainly along the *a* axis of the crystal. **b**, Schematic illustration of the Néel vector, defined as $\mathbf{L} = \mathbf{M}_1 - \mathbf{M}_2$, where $\mathbf{M}_1$ and $\mathbf{M}_2$ represent two oppositely aligned spins. **c**, Optical microscopy image of exfoliated $NiPS_3$ flakes on a silicon substrate with a 285 nm SiO_2 layer, where different colours represent the samples with different thicknesses. The trilayer flake is marked by the white dashed line, and the inset is its height profile along the white solid line. **d**, PL spectra from the bulk and the trilayer $NiPS_3$ flake under 568 nm continuous-wave laser excitation at 5 K. The sharp PL peak is labelled as X. The inset shows a high-resolution spectrum of peak X with a FWHM of ~330 μeV in bulk $NiPS_3$.

both are close to the band gap energy (~1.5 eV) of $NiPS_3$ (refs. [18,21]). By contrast, such a sharp emission is absent in bilayer flakes (Supplementary Fig. 2a). Here we focus on peak X, while other peaks in close proximity are discussed in Supplementary Discussion Sections 5 and 6. The intensity of peak X clearly decreases with the increase of temperature and vanishes at $T > 120$ K, which is ~30 K lower than the T_N of $NiPS_3$ (Fig. 2a). Moreover, as the temperature decreases from 120 to 20 K, the integrated PL intensity exhibits gradual variation (Fig. 2b). This behaviour of peak X is distinct from most phenomena induced by a magnetic phase transition, which usually follow an exponential function and exhibit a non-differentiable inflection point at T_N[13,14]. Our experimental results imply that the disappearance of peak X at a high temperature is not directly caused by the magnetic phase transition. The measured time-resolved decay curve of peak X, after deconvolution with the instrument response function, indicates an upper bound of a lifetime of ~10 ps (Supplementary Fig. 3d). As a comparison, peak X exhibits a full width at half maximum (FWHM) of ~330 μeV, corresponding to a lower limit for a lifetime of ~2 ps. Therefore, the lifetime of peak X is estimated to be on the order of picoseconds.

As one of the appealing features of peak X, the exceptionally narrow linewidth raises concern over whether the emission originates from isolated structural defects in the crystal (inset in Fig. 1d)[22]. However, this possibility can be ruled out based on the linear dependence of PL intensity on the excitation power up to 2.5 mW (Fig. 2c)[23] and the emission homogeneity over several square micrometres of area on flakes with the same thickness (Supplementary Fig. 3c)[24–26]. Particularly, we observed an absorption peak at ~1.480 eV, which is close to PL peak X at ~1.476 eV (Fig. 2d). These two peaks exhibit a similar temperature dependence, suggesting they share a similar origin (Supplementary Fig. 4). The noticeable absorption also strongly excludes isolated defect states as the origin of the emission, as the corresponding absorption is generally invisible due to the limited density of states in crystals[23].

In addition, our data reveals a correlation between the sharp peak X with both the magnetic and electronic properties of $NiPS_3$, further suggesting that it stems from an intrinsic transition of the material. First, the layer-dependent data show that the PL intensity rapidly decreases with a reduction of layer number in the few-layer region, and finally disappears in the bilayer sample (Supplementary Fig. 2). The suppression of PL intensity in thin flakes could be the consequence of the suppression of magnetic ordering, which has been previously established[15]. Second, peak X is located near the absorption edge (~1.5 eV) of $NiPS_3$, suggesting that it is possibly correlated to the band edge transition of the material. The calculated electronic band structure, from density functional theory (DFT) including a Hubbard *U* parameter on the Ni atoms, indicates an indirect band gap of 1.55 eV in bulk $NiPS_3$ (Supplementary Fig. 5). The density of states shows that the low-lying conduction band is mainly composed of Ni *d*-orbital electrons, while the high-lying valence bands are predominantly S *p*-orbital electrons. Therefore, we speculate that peak X originates from the transition involving these two types of electrons in $NiPS_3$. A recent investigation reporting a similar phenomenon from $NiPS_3$ attributes the sharp emission to a transition between a Zhang–Rice triplet and a Zhang–Rice singlet[27].

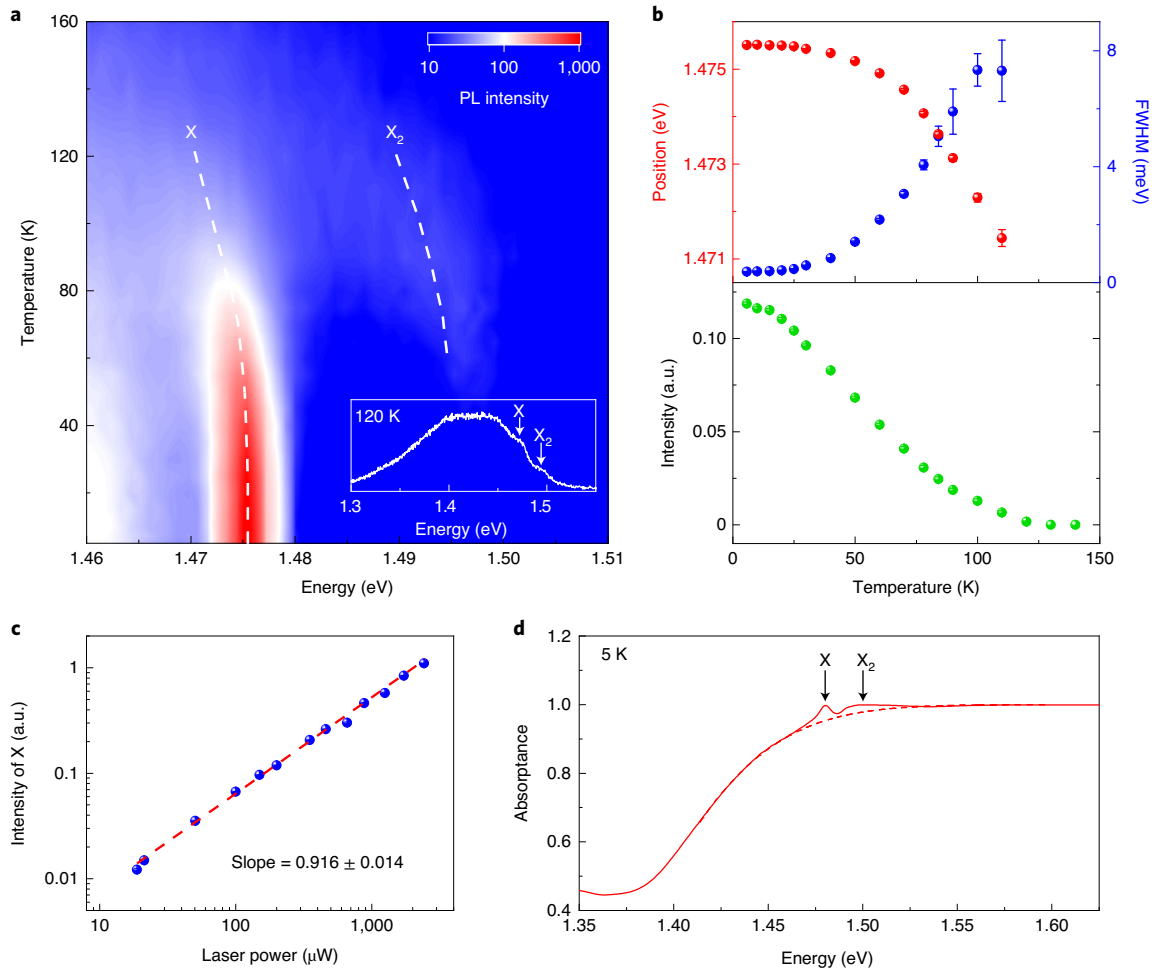

Fig. 2 | Characterization of sharp peak X in $NiPS_3$. **a**, Temperature-dependent PL colour map under 568 nm laser excitation. Two PL peaks (labelled X and X_2) are observed. The inset is the spectrum at 120 K. **b**, Extracted FWHM, peak position and integrated intensity of peak X as a function of temperature under 568 nm excitation. **c**, Excitation-power-dependent intensity of peak X excited by a 568 nm laser. The slope of linear fitting indicates the linear dependence of intensity on the excitation power in the range from 17 μW to 2.5 mW. **d**, Absorptance spectrum of bulk $NiPS_3$ at 5 K. Two absorption peaks located at the band edge are assigned to the X and X_2 peaks.

Such a transition represents a variation of the relative spins between the holes in the Ni *d* orbital and S *p* orbital, that is, the relative spins between the unpaired electrons in the Ni *d* orbital and S *p* orbital[27,28], aligning well with our speculation. However, it remains ambiguous, but fundamentally important to understand, why an intrinsic transition can generate such a narrow emission at hundreds of microelectronvolts. We consider that this feature is possibly a consequence of the trapped states in the crystal due to a self-doping effect (Supplementary Discussion Section 4).

Linearly polarized PL in the antiferromagnetic phase

More importantly, since $NiPS_3$ is a vdW crystal with intrinsic antiferromagnetism, the observation of sharp emission provides an excellent platform for studying magneto-optics in quasi-2D systems. Specifically, it is extremely intriguing to explore whether peak X could couple to the spin structure in the material to a great extent. To this end, we have measured the polarization-dependent PL of $NiPS_3$ in two configurations (Supplementary Fig. 7). In the first configuration, we rotate the incident laser polarization (P_{in}) and measure the total PL intensity of peak X with a fixed collection polarization (P_{col}). We do not observe a clear dependence of the PL on P_{in} (Fig. 3a). The isotropy of the PL intensity is due to the weak anisotropy of optical absorption above the band gap energy.

In the second configuration, we maintain the same excitation laser polarization, while we measure the PL of peak X at different collection light polarization (P_{col}). Remarkably, we find that the measured PL varies with P_{col} (Fig. 3a). The PL intensity reaches a maximum (minimum) when P_{col} is perpendicular (parallel) to the *a* axis, which is determined by selected-area electron diffraction (Supplementary Fig. 8). From the bulk down to samples of a few layers, a similar phenomenon is observed and the PL intensity can be fitted by a sinusoidal function: $I(\theta) = I_0 + I_1 \sin^2\theta$, where θ is the angle between the PL polarization and the *a* axis of $NiPS_3$, and I_0 and I_1 are fitting constants (dashed lines in Fig. 3a and Supplementary Fig. 9).

To investigate the origin of the linear polarization, we first conduct the temperature-dependent PL polarization measurement (Fig. 3b). We define the PL linear polarization degree, $\rho = (I_b - I_a)/(I_b + I_a)$, where I_a (I_b) is the PL peak intensity when P_{col} is parallel to the *a* axis (*b* axis). We find that ρ is ~70% at $T < 70$ K, and drops with increasing temperature (Fig. 3c). The temperature-dependent PL polarization degree is fitted well by $\rho(T) \approx \left|1 - \frac{T}{T_N}\right|^{2\beta_{PL}}$, where β_{PL} is a critical exponent indicating the decay trend near the phase transition temperature[29]. We obtain $\beta_{PL} = 0.26 \pm 0.05$, which is in good agreement with the similar exponent $\beta = 0.23$–0.26 for the temperature-dependent magnetic intensity in 2D XY type systems[30,31].

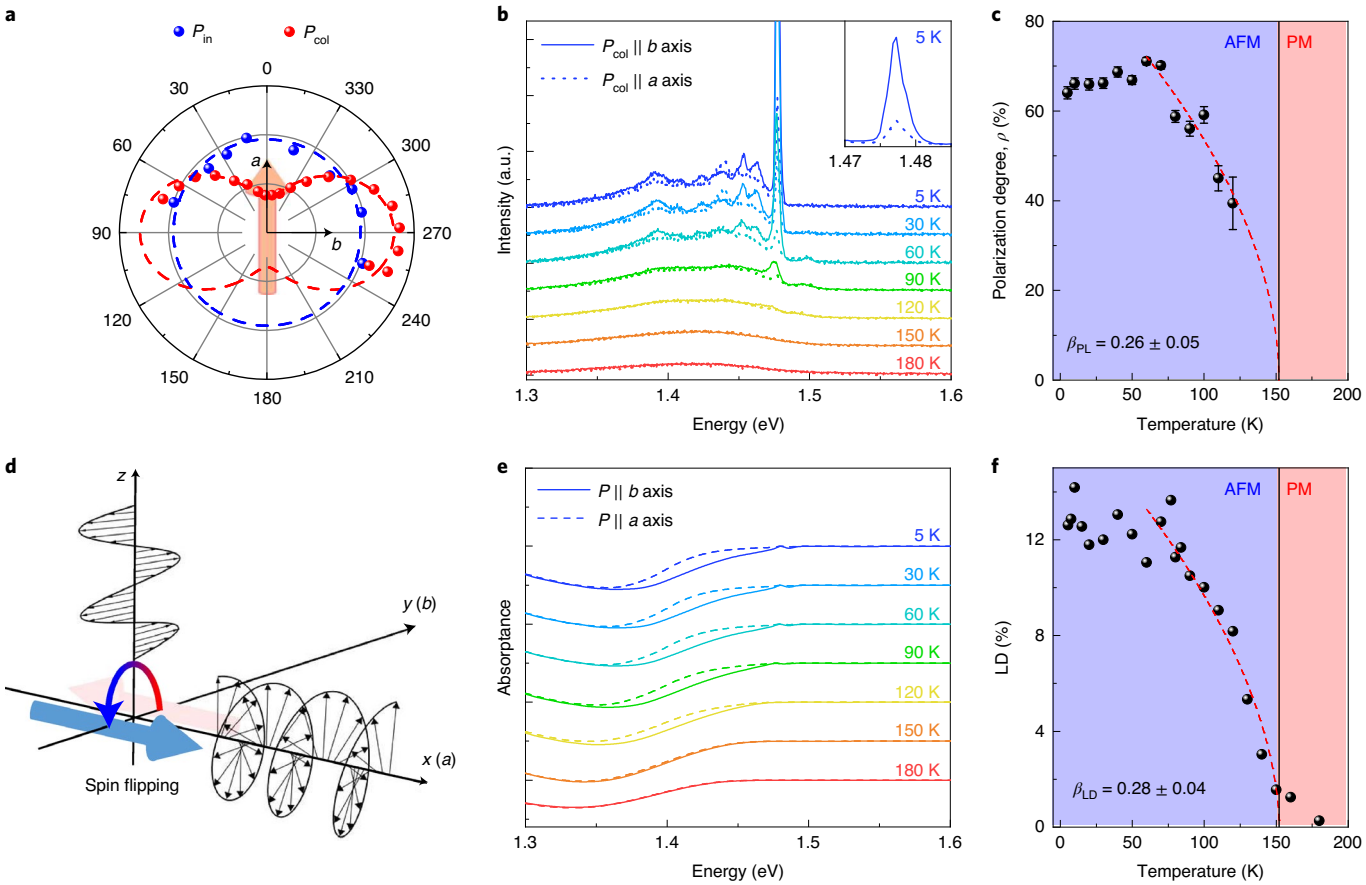

Fig. 3 | Spin-induced linear polarization of PL and absorption anisotropy in $NiPS_3$. **a**, PL intensity as a function of the incident laser polarization (blue) and collection polarization (red) at 5 K. The crystal orientations (*a* and *b* axes) and Néel vector orientation have been labelled by thin black and thick orange arrows, respectively. **b**, Temperature-dependent PL spectra under 568 nm excitation in two polarization configurations, where the collection light polarization are parallel to the *b* and *a* axes, respectively. The inset shows the linear polarization of peak X at 5 K. **c**, PL polarization degree ($\rho = (I_b - I_a)/(I_b + I_a)$) as a function of temperature. The dashed line is the fitting using the formula, $\rho(T) \sim \left|1 - \frac{T}{T_N}\right|^{2\beta_{PL}}$, where $\beta_{PL} = 0.26 \pm 0.05$. **d**, Schematic illustration of the origin of the linear polarization of peak X. The spin flipping from the red to the blue thick arrow along *x* activates an electric dipole oscillation in the *y*–*z* plane, which generates circular polarized photons along the *x* direction and linear polarized photons along the *z* direction. **e**, Temperature-dependent absorptance spectra of the $NiPS_3$ bulk crystal in two polarization configurations, where the light polarizations are parallel to the *b* and *a* axes, respectively. **f**, LD (LD = $(A_a - A_b)/(A_a + A_b)$) as a function of temperature. The dashed line is the fitting using the formula, LD $(T) \sim \left|1 - \frac{T}{T_N}\right|^{2\beta_{LD}}$, where $\beta_{LD} = 0.28 \pm 0.04$. The blue and red areas in **c** and **f** represent the antiferromagnetic (AFM) and the paramagnetic (PM) phases, respectively.

This agreement suggests that the linear polarization of peak X in $NiPS_3$ arises from the ordered spins.

As shown in Fig. 1a, the anisotropic spin structure of $NiPS_3$ is mainly controlled by two factors—Néel vector orientation and ferromagnetic spin chain direction, which are both along the *a* axis. A fundamental question is which one gives rise to the linear polarization of peak X. As peak X is reported to originate from the transition between a Zhang–Rice triplet and a Zhang–Rice singlet, the relative spin orientation of the unpaired electrons in the Ni *d* orbital and S *p* orbital changes from being the same direction to opposite directions during the transition[27]. Since the initial spins of unpaired electrons are known to be along the *a* axis of the crystal, the spin flipping causes a spin quantum number difference, ΔS, along the *a* axis. Therefore, the generated electric dipole should be rotating in the plane perpendicular to the *a* axis, and thus an emitted photon carries an angular momentum, *J*, along the *a* axis to conserve the total quantum number in this direction. Meanwhile, this electric dipole will emit photons in the equatorial plane with a linear polarization perpendicular to the polar direction (Fig. 3d). As a result, in our case of $NiPS_3$, peak X exhibits a linear polarization perpendicular to the Néel vector when we collect the signal along the surface normal.

In the presence of spin–photon coupling, it is of great importance to investigate the magneto-optical properties of $NiPS_3$ across the T_N of ~152 K. Unfortunately, peak X vanishes at a characteristic temperature of ~120 K, which is ~30 K below the T_N. Nevertheless, the optical absorption of $NiPS_3$ also exhibits clear anisotropy near the band edge (~1.5 eV) in the antiferromagnetic phase (Fig. 3e). The linear dichroism (LD) of $NiPS_3$ is obtained by the formula $LD = (A_a - A_b)/(A_a + A_b)$, where A_a (A_b) is the absorptance when the polarization of the incident white light is parallel to the *a* axis (*b* axis; Fig. 3f). LD stays around 12% when $T < 70$ K and dramatically decays with increasing temperature. Moreover, LD reaches a minimum around T_N, suggesting that the anisotropy of the absorption arises from the anisotropic spin structure. The temperature-dependent LD is fitted by $LD(T) \sim \left|1 - \frac{T}{T_N}\right|^{2\beta_{LD}}$, where $\beta_{LD} = 0.28 \pm 0.04$ matches well with β_{PL} and the reported β in the other 2D XY type spin systems[29,32]. Magnetic LD is a common phenomenon in many ferromagnetic and antiferromagnetic materials with spins aligning in-plane[29]. Due to the magneto-optical effect, the optical absorption coefficient changes for different light polarizations. Consequently, the electric field of transmitted and reflected light is suppressed

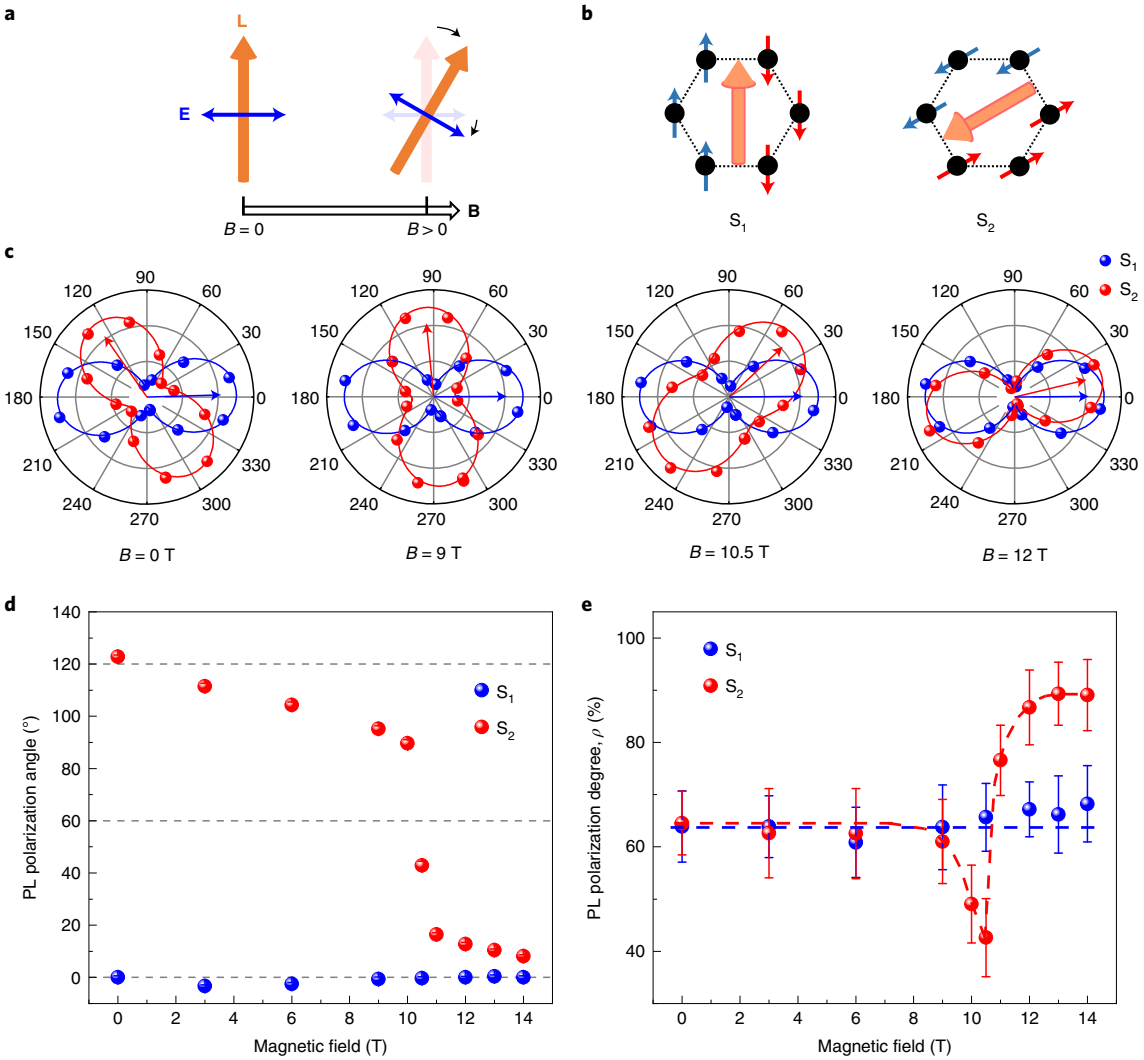

Fig. 4 | Magnetic manipulation of PL polarization in the Voigt geometry. a, Illustration of rotating linear polarization of peak X in an applied in-plane field. The solid orange, solid blue and hollow black arrows represent the Néel vector (**L**), electric dipole oscillator (**E**) and applied field (**B**), respectively. **b**, Illustrated diagram of the initial alignments of spins (thick blue and red arrows) and Néel vectors (thick orange arrows) in two samples. The crystal orientations (that is, the *a* axis) of two bulk $NiPS_3$ samples (S_1 and S_2) are 120° from each other. **c**, Integrated PL intensity of peak X as a function of collection polarization angle on S_1 and S_2 at different magnetic fields ($B = 0$, 9, 10.5 and 12 T). **d**, PL polarization angles of sample S_1 and S_2 as a function of the in-plane magnetic field. The black dashed lines are the possible zigzag spin chain directions. **e**, Polarization degree, $\rho = (I_b - I_a)/(I_b + I_a)$, as a function of the applied magnetic field for S_1 and S_2. The results show a magnetic phase transition around $B = 10.5$ T.

along the spin orientation, resulting in a weak polarization for depolarized light or a Voigt effect for linearly polarized light[32]. The magnetic LD near the band edge and PL linear polarization observed in $NiPS_3$ crystals indicate that the spin structure strongly regulates the optical transition. A magnetic LD of ~12% in $NiPS_3$ is rather strong, compared to that in common magnetic materials, where the magnetic LD is typically smaller than 1% (refs. [32,33]). In particular, peak X features an even larger polarization degree of ~70%, suggesting a strong coupling to spins. Additionally, the PL spectra in the range of 1.35–1.5 eV show distinct polarized character at different emission energies, in stark opposition to the idea that the linear polarization of PL peaks stems from the anisotropic reabsorption of the material (Supplementary Fig. 10).

Magnetic manipulation of emitted photons

Although the temperature-dependent study provides remarkable evidence that the linear polarization of peak X arises from the spin structure, the underlying mechanism of the coupling between the transition and spin is still controversial[27]. In particular, the fact that the ferromagnetic spin chain and the Néel vector align along the same direction (that is, the *a* axis) leads to difficulty identifying their contributions to the polarization of peak X experimentally. Based on the XY nature of spins in $NiPS_3$ at low temperatures, one strategy to avoid this complication is to apply an in-plane field to rotate the Néel vector away from the spin chain direction[20]. As shown in the model we proposed, when the Néel vector rotates in the *a*–*b* plane, the spin flipping should result in a ΔS along the new direction of the Néel vector, which is away from the *a* axis (Fig. 4a). Meanwhile, the generated dipole oscillator remains perpendicular to the ΔS vector. Therefore, the polarization of peak X also rotates away from the *b* axis, with the same angle as the Néel vector rotation. We conduct a magneto-optical study on $NiPS_3$ in the Voigt geometry. We mount two bulk $NiPS_3$ samples (labelled S_1 and S_2) inside a magnetic cell. Their crystal orientations (that is, the *a* axis) are rotated by 120° relative to each other (Fig. 4b). As a result, the PL polarization of peak X from samples S_1 and S_2 is off by 120° at zero applied magnetic

field (Fig. 4c), consistent with our results in Fig. 3a. Then, we apply an in-plane magnetic field (B) up to 14 T and conduct the polarized PL measurements (Fig. 4c). Remarkably, we achieve the manipulation of the polarization of the sharp emission. The polarization of peak X from S_2 shows a clear rotation with respect to that of S_1 when the magnetic field increases and finally orients in the same direction as the PL polarization from S_1 at $B = 14$ T. The result provides unambiguous evidence that the polarization peak X is determined by the spin structures, rather than by the weak crystalline anisotropy from the layer stacking.

We compare the PL polarization angles for samples S_1 and S_2 at different B fields (Fig. 4d). The difference between the PL polarization angles of two samples continuously varies when the applied field increases over the ranges of ~0–10 T and ~11–14 T, and dramatically changes at $B = \sim 10.5$ T. Since the ferromagnetic spin chain can only align along the zigzag directions of the crystal, the hexagonal lattice structure of $NiPS_3$ limits the minimum rotation of the spin chain to 60°, which is labelled as horizontal black dashed lines in Fig. 4d. By contrast, the Néel vector in $NiPS_3$ is able to align along any directions in the plane, as we observed in the experiments, due to its XY behaviour at low temperatures[15]. We also notice that if the spin chains could rotate with a step of 60° in small magnetic domains, a collective effect in the region of the laser spot would also result in a continuous rotation of PL polarization due to an increasing percentage of domain areas with a changed spin chain. However, this possibility cannot be achieved, since such an intermediate phase containing multiple spin chain states would cause a reduction of the polarization degree, which contradicts the unchanged polarization degree of S_2 from 0 to 9 T observed in our measurements (Fig. 4e). The sudden drop of the polarization degree at ~10.5 T indicates a field-induced magnetic phase transition from an antiferromagnetic state to another antiferromagnetic state, similar to the case in $MnPS_3$ (refs. [34,35]). Therefore, our magneto-optical measurements provide unambiguous evidence that the polarization of peak X is determined by the Néel vector direction instead of the spin chain direction in $NiPS_3$.

Conclusion

Benefiting from the spin-correlated emission in $NiPS_3$, the Néel vector orientation can be optically detected as perpendicular to the PL polarization. Even though the manipulation of the PL polarization was only demonstrated in bulk $NiPS_3$, we anticipate similar results with few-layer flakes, in which the linearly polarized emission has also been demonstrated (Supplementary Fig. 9). Our report on the spin-correlated PL in the vdW antiferromagnet $NiPS_3$ will greatly advance future fundamental research in magnetism and magneto-optics. Most existing optical spin-probe techniques for antiferromagnets are technically difficult to conduct and not suitable for ultrathin samples, since they require an ultrafast laser to induce the thermal or magnetic perturbation[33,36], and the amplitudes of the signals are proportional to the thickness of the samples[5,33]. By contrast, the spin-induced polarization of PL demonstrated here using a steady-state microspectroscopy method offers an easy, fast, nondestructive strategy to determine the Néel vector orientation and investigate the spin properties of atomically thin antiferromagnets. We anticipate that this mechanism of spin–photon coupling will stimulate future theoretical and experimental studies in the field, promoting the development of opto-spintronic devices and magnetic quantum information technology.

Online content

Any methods, additional references, Nature Research reporting summaries, source data, extended data, supplementary information, acknowledgements, peer review information; details of author contributions and competing interests; and statements of data and code availability are available at https://doi.org/10.1038/s41563-021-00968-7.

Received: 13 June 2020; Accepted: 24 February 2021;
Published online: 26 April 2021

References

1. Huang, B. et al. Layer-dependent ferromagnetism in a van der Waals crystal down to the monolayer limit. *Nature* **546**, 270–273 (2017).
2. Gong, C. et al. Discovery of intrinsic ferromagnetism in two-dimensional van der Waals crystals. *Nature* **546**, 265–269 (2017).
3. Burch, K. S., Mandrus, D. & Park, J.-G. Magnetism in two-dimensional van der Waals materials. *Nature* **563**, 47–52 (2018).
4. Seyler, K. L. et al. Ligand-field helical luminescence in a 2D ferromagnetic insulator. *Nat. Phys.* **14**, 277–281 (2018).
5. Němec, P., Fiebig, M., Kampfrath, T. & Kimel, A. V. Antiferromagnetic opto-spintronics. *Nat. Phys.* **14**, 229–241 (2018).
6. Jungwirth, T., Marti, X., Wadley, P. & Wunderlich, J. Antiferromagnetic spintronics. *Nat. Nanotechnol.* **11**, 231–241 (2016).
7. Kirilyuk, A., Kimel, A. V. & Rasing, T. Ultrafast optical manipulation of magnetic order. *Rev. Mod. Phys.* **82**, 2731–2784 (2010).
8. Kampfrath, T. et al. Coherent terahertz control of antiferromagnetic spin waves. *Nat. Photonics* **5**, 31–34 (2011).
9. Kriegner, D. et al. Multiple-stable anisotropic magnetoresistance memory in antiferromagnetic MnTe. *Nat. Commun.* **7**, 11623 (2016).
10. Olejník, K. et al. Antiferromagnetic CuMnAs multi-level memory cell with microelectronic compatibility. *Nat. Commun.* **8**, 15434 (2017).
11. Marti, X. et al. Room-temperature antiferromagnetic memory resistor. *Nat. Mater.* **13**, 367–374 (2014).
12. Wadley, P. et al. Electrical switching of an antiferromagnet. *Science* **351**, 587–590 (2016).
13. Wang, X. et al. Raman spectroscopy of atomically thin two-dimensional magnetic iron phosphorus trisulfide ($FePS_3$) crystals. *2D Mater.* **3**, 031009 (2016).
14. Lee, J.-U. et al. Ising-type magnetic ordering in atomically thin $FePS_3$. *Nano Lett.* **16**, 7433–7438 (2016).
15. Kim, K. et al. Suppression of magnetic ordering in XXZ-type antiferromagnetic monolayer $NiPS_3$. *Nat. Commun.* **10**, 345 (2019).
16. Chu, H. et al. Linear magnetoelectric phase in ultrathin $MnPS_3$ probed by optical second harmonic generation. *Phys. Rev. Lett.* **124**, 027601 (2020).
17. Sun, Z. et al. Giant nonreciprocal second-harmonic generation from antiferromagnetic bilayer CrI_3. *Nature* **572**, 497–501 (2019).
18. Du, K. et al. Weak van der Waals stacking, wide-range band gap, and Raman study on ultrathin layers of metal phosphorus trichalcogenides. *ACS Nano* **10**, 1738–1743 (2016).
19. Kuo, C.-T. et al. Exfoliation and Raman spectroscopic fingerprint of few-layer $NiPS_3$ van der Waals crystals. *Sci. Rep.* **6**, 20904 (2016).
20. Wildes, A. R. et al. Magnetic structure of the quasi-two-dimensional antiferromagnet $NiPS_3$. *Phys. Rev. B* **92**, 224408 (2015).
21. Piacentini, M., Khumalo, F. S., Olson, C. G., Anderegg, J. W. & Lynch, D. W. Optical transitions, XPS, electronic states in $NiPS_3$. *Chem. Phys.* **65**, 289–304 (1982).
22. Liu, X. & Hersam, M. C. 2D materials for quantum information science. *Nat. Rev. Mater.* **4**, 669–684 (2019).
23. Schmidt, T., Lischka, K. & Zulehner, W. Excitation-power dependence of the near-band-edge photoluminescence of semiconductors. *Phys. Rev. B* **45**, 8989–8994 (1992).
24. Gao, W. B., Fallahi, P., Togan, E., Miguel-Sanchez, J. & Imamoglu, A. Observation of entanglement between a quantum dot spin and a single photon. *Nature* **491**, 426–430 (2012).
25. Jungwirth, N. R. & Fuchs, G. D. Optical absorption and emission mechanisms of single defects in hexagonal boron nitride. *Phys. Rev. Lett.* **119**, 057401 (2017).
26. Tonndorf, P. et al. Single-photon emitters in GaSe. *2D Mater.* **4**, 021010 (2017).
27. Kang, S. et al. Coherent many-body exciton in van der Waals antiferromagnet $NiPS_3$. *Nature* **583**, 785–789 (2020).
28. Zhang, F. C. & Rice, T. M. Effective Hamiltonian for the superconducting Cu oxides. *Phys. Rev. B* **37**, 3759–3761 (1988).
29. Ferre, J. & Gehring, G. A. Linear optical birefringence of magnetic crystals. *Rep. Prog. Phys.* **47**, 513–611 (1984).
30. Bramwell, S. T. & Holdsworth, P. C. W. Magnetization and universal sub-critical behaviour in two-dimensional XY magnets. *J. Phys. Condens. Matter* **5**, L53–L59 (1993).
31. Bramwell, S. T., Day, P., Hutchings, M. T., Thorne, J. R. G. & Visser, D. Neutron scattering and optical study of the magnetic properties of the two-dimensional ionic rubidium chromium bromide chloride ferromagnets Rb_2CrCl_3Br and $Rb_2CrCl_2Br_2$. *Inorg. Chem.* **25**, 417–421 (1986).

32. Tesařová, N. et al. Systematic study of magnetic linear dichroism and birefringence in (Ga,Mn)As. *Phys. Rev. B* **89**, 085203 (2014).
33. Saidl, V. et al. Optical determination of the Néel vector in a CuMnAs thin-film antiferromagnet. *Nat. Photon.* **11**, 91–96 (2017).
34. Chittari, B. L. et al. Electronic and magnetic properties of single-layer MPX_3 metal phosphorous trichalcogenides. *Phys. Rev. B* **94**, 184428 (2016).
35. Long, G. et al. Persistence of magnetism in atomically thin $MnPS_3$ crystals. *Nano Lett.* **20**, 2452–2459 (2020).
36. Kimel, A. V. et al. Ultrafast non-thermal control of magnetization by instantaneous photomagnetic pulses. *Nature* **435**, 655–657 (2005).

Methods

Sample preparation. $NiPS_3$ single crystals were grown using a chemical vapour transport method[18]. A stoichiometric amount of high-purity elements (mole ratio Ni/P/S = 1:1:3, ~1 g in total) and iodine (~10–20 mg) as a transport agent were sealed into a quartz ampule and kept in a two-zone furnace (650–600 °C). The length of the quartz ampule was about 16 cm with a 13 mm external diameter. The pressure inside the ampule was pumped down to 1×10^{-4} torr. After 1 week of heating, the ampule was cooled to room temperature, with bulk crystals appearing in the lower temperature end. The purity of the synthesized sample was confirmed by a series of characterizations. The powder X-ray diffraction data were collected on a Bruker D8 Discover diffractometer with Cu K_α radiation of wavelength $\lambda = 1.5418$ Å at 40 kV and 40 mA. Elemental analysis experiments were conducted using energy dispersive spectroscopy attached to a field emission scanning electron microscope (Zeiss Supra 55). Transmission electron microscopy measurements were performed on a FEI Tecnai Osiris transmission electron microscope, operating at a 200 keV accelerating voltage. Selected-area electron diffraction was measured on a JEOL 2100 transmission electron microscope. The selected-area electron diffraction simulation was performed through STEM_CELL software.

Few-layer $NiPS_3$ flakes were prepared on Si substrates with a 285 nm SiO_2 layer by mechanical exfoliation from a bulk single crystal. The morphology and thickness of the exfoliated flakes were characterized using optical microscopy (Nikon DS-Ri2) and atomic force microscopy (Bruker Dimension 3000) in a tapping mode.

Raman scattering, PL and absorptance spectroscopy. Optical measurements were carried out on a micro-Raman spectrometer (Horiba-JY T64000), and the signal was collected through a ×50 long-working-distance objective. A cryostat (Cryo Industry of America) was used to provide a vacuum environment and a continuous temperature from 5 to 300 K by liquid helium flow. The Raman scattering measurement was performed using a triple-grating mode with 1,800 g mm^{-1} gratings, and a 568 nm laser line from a Kr^+/Ar^+ ion laser (Coherent Innova 70C Spectrum) was used to excite the sample. Micro-PL and micro-absorption measurements were carried out using a single-grating mode. For PL, 458 and 568 nm laser lines from the Kr^+/Ar^+ ion laser were used to excite the sample. The backscattered signal was dispersed with a 150 g mm^{-1} or 1,800 g mm^{-1} grating. A stabilized tungsten–halogen white-light source (SLS201L, Thorlabs) was used to irradiate the bulk sample from the bottom in the micro-absorption measurements. The signal from an effective area ~5 μm in diameter was collected. The absorptance spectra were determined by $A(\lambda) = 1 - Tr(\lambda)/Tr_0(\lambda)$, where $Tr(Tr_0)$ is the intensity of light transmitted through the sample (substrate).

Polarization-dependent PL and magneto-PL measurement. The polarization-dependent PL and magneto-PL experiments were performed in the National High Magnetic Field Lab. In the polarization-dependent PL measurement, a 488 nm laser was used to excite the bulk crystal and exfoliated flakes. A ×50 long-working-distance objective was used to focus the excitation onto the sample and collect the PL signal. The magneto-optical experiments were performed with a 14 T d.c. magnet on the bulk crystal. A 532 nm continuous-wave laser was used to excite the sample. The sample was positioned vertically inside the magnetic cell with the surface parallel to the applied magnetic field. A mirror was set between the objective and sample with an angle of 45° to change the optical path by 90°. A ×10 objective was used to focus the excitation onto the sample and collect the PL signal. For both the polarization-dependent and magnetic-field-dependent experiments, the PL signal was filtered by an analyser, subsequently collected by a multi-mode optical fibre and measured by a spectrometer with a charge-coupled device camera (Princeton Instruments, IsoPlane 320).

Time-resolved PL measurement. The time-resolved PL experiment was conducted using a time-correlated single photon counting technique. The excitation laser pulses came from an oscillator (Light Conversion, Pharos) with 1,030 nm output wavelength, 80 MHz repetition rate and 90 fs pulse duration. The second harmonic (515 nm wavelength) of the laser was used to excite the samples. The PL signal was spectrally dispersed and filtered by a grating monochromator before detection by a photodiode.

DFT calculations. DFT calculations were performed using the Vienna Ab initio Simulation Package (VASP)[37–40]. We utilized the local density approximation with a Hubbard U parameter of 4.0 eV on each nickel atom[34,41] to describe the correlated behaviour of the d electrons, using the simplified, rotationally invariant Dudarev approach implemented in VASP[42]. Projector augmented wave potentials describe the core and nuclei of atoms, with 10, 5 and 6 electrons treated explicitly for Ni, P and S, respectively[43,44]. The k-point mesh for self-consistent field and structural optimization was $4\times7\times5$, sufficient to converge the total energy to 1 meV per atom. Additionally, for structural optimization we used a cut-off energy for the planewave basis set of 470 eV and a threshold of 1 meV Å^{-1} for all forces. To determine the magnetic state of the $NiPS_3$, we initialized the system with two types of antiferromagnetic and one ferromagnetic state, with an initial magnetic moment of 3.0 or −3.0 assigned to each nickel atom, and determined the lowest energy structure. In agreement with previous studies, we found that antiferromagnetically coupled 'zigzag' stripes of aligned spins, described in Fig. 1a, were the lowest energy structure[45]. The other structures considered were a ferromagnetic configuration and an antiferromagnetic configuration in which spins alternated between nearest neighbours.

To calculate the band structure and density of states, we used a k path between 12 high-symmetry points in the Brillouin zone[46] with 10 k points along each segment (or 20, when considering spin–orbit coupling). We checked the effect of spin–orbit coupling by performing non-collinear magnetic structure calculations in VASP[47] starting from both the DFT relaxed geometry and the lattice parameters from experiment. In both cases, spin–orbit coupling resulted in narrow band splitting (<0.01 eV) in some segments of the valance and conduction bands.

Data availability

Source data are provided with this paper. All other data that support results in this article are available from the corresponding authors on reasonable request.

References

37. Kresse, G. & Hafner, J. *Ab initio* molecular dynamics for liquid metals. *Phys. Rev. B* **47**, 558–561 (1993).
38. Kresse, G. & Hafner, J. *Ab initio* molecular-dynamics simulation of the liquid-metal–amorphous-semiconductor transition in germanium. *Phys. Rev. B* **49**, 14251–14269 (1994).
39. Kresse, G. & Furthmüller, J. Efficiency of ab-initio total energy calculations for metals and semiconductors using a plane-wave basis set. *Comput. Mater. Sci.* **6**, 15–50 (1996).
40. Kresse, G. & Furthmüller, J. Efficient iterative schemes for *ab initio* total-energy calculations using a plane-wave basis set. *Phys. Rev. B* **54**, 11169–11186 (1996).
41. Kim, S. Y. et al. Charge-spin correlation in van der Waals antiferromagnet $NiPS_3$. *Phys. Rev. Lett.* **120**, 136402 (2018).
42. Dudarev, S. L., Botton, G. A., Savrasov, S. Y., Humphreys, C. J. & Sutton, A. P. Electron-energy-loss spectra and the structural stability of nickel oxide: an LSDA+U study. *Phys. Rev. B* **57**, 1505–1509 (1998).
43. Kresse, G. & Hafner, J. Norm-conserving and ultrasoft pseudopotentials for first-row and transition elements. *J. Phys. Condens. Matter* **6**, 8245–8257 (1994).
44. Kresse, G. & Joubert, D. From ultrasoft pseudopotentials to the projector augmented-wave method. *Phys. Rev. B* **59**, 1758–1775 (1999).
45. Kurita, N. & Nakao, K. Band structure of magnetic layered semiconductor $NiPS_3$. *J. Phys. Soc. Jpn* **58**, 232–243 (1989
46. Setyawan, W. & Curtarolo, S. High-Throughput Electronic Band StructureCalculations: Challenges and Tools. *Comput. Mater. Sci.* **49**, 299–312, (2010).
47. Steiner, S. et al. Calculation of the Magnetic Anisotropy with Projected-AugmentedWave Methodology and the Case Study of Disordered Fe1−xCox Alloys. *Phys. Rev. B* **93**, 224425, (2016).

Acknowledgements

This material is based upon work supported by the National Science Foundation under grant no. 1945364. X.W. and X.L. acknowledge the financial support from Boston University and the Photonics Center at Boston University. The transmission electron microscopy imaging was performed at the Center for Nanoscale Systems, a member of the National Nanotechnology Coordinated Infrastructure Network, which is supported by the National Science Foundation under award no. 1541959. The Center for Nanoscale Systems is part of Harvard University. A.C. and S.S. acknowledge financial support from the US Department of Energy, Office of Science, Basic Energy Sciences Early Career Program under award no. DE-SC0018080. We acknowledge the computational resources through the Extreme Science and Engineering Discovery Environment, which is supported by National Science Foundation grant no. ACI-1548562; and the National Energy Research Scientific Computing Center, a US Department of Energy Office of Science User Facility supported by the Office of Science of the US Department of Energy under contract no. DE-AC02-05CH11231. Z.L. and D.S. acknowledge support from the US Department of Energy (no. DE-FG02-07ER46451) for high-field magnetospectroscopy measurements performed at National High Magnetic Field Laboratory, which is supported by the National Science Foundation through NSF/DMR-1644779 and the state of Florida. C.H.L. acknowledges support from the American Chemical Society Petroleum Research Fund (ACS PRF No. 61640-ND6).

Author contributions

X.W. and X.L. conceived the experiment. X.W. carried out PL and absorption measurements. X.W., J.C. and Z.L. conducted the magneto-PL measurements with assistance from D.S. at the National High Magnetic Field Laboratory. J.C. and X.W.

prepared samples. J.C., H.K., T.L. and Q.T. carried out the sample characterization. A.C. and S.S. performed theoretical calculations. M.W. performed the time-resolved PL measurement under the supervision of C.H.L.; X.W. and X.L. performed the analysis and interpretation of the data. All authors assisted in the interpretation of data and contributed to the writing of the manuscript.

Competing interests

The authors declare no competing interests.

Additional information

Supplementary information The online version contains supplementary material available at https://doi.org/10.1038/s41563-021-00968-7.

Correspondence and requests for materials should be addressed to X.W. or X.L.

Peer review information *Nature Materials* thanks the anonymous reviewers for their contribution to the peer review of this work.